

# High-Temperature Bending Fatigue Properties of Oxide Dispersion-Strengthened Platinum–Rhodium Alloy under High Axial Stress

A. Niwa<sup>a</sup>, Y. Akita<sup>a</sup>, K. Enomoto<sup>b</sup>, R. Aoyama<sup>b</sup>, H. Akebono<sup>b</sup>, A. Sugeta<sup>b</sup>

<sup>a</sup> *Innovative Technology Laboratories, AGC Inc.*

<sup>b</sup> *Department of Mechanical Science and Engineering, Hiroshima University*

## Abstract

In this study, high-temperature bending fatigue tests were carried out using an oxide dispersion-strengthened platinum-rhodium alloy at 1400 °C with a relatively high axial stress. At a low stress amplitude, creep damage progressed throughout the cross-section of the sample due to axial stress. However, at a high stress amplitude, creep damage progressed only in the central part of the direction of thickness and fracturing originated from inside the sample. Elastic-plastic creep analysis also indicated that high tensile stress remained inside the sample due to the yielding near the surface. The fact that the life is determined by the creep due to the stress generated inside of the material is useful for life prediction.

## 1. Introduction

Platinum alloys are used widely in industrial applications such as fuel cell electrodes and catalysts for removing harmful substances from automobile exhaust gas [1]. They are also employed widely in glass manufacturing processes in components such as melting crucibles and stirrers because they exhibit excellent resistance to molten glass at high temperatures as well as high oxidation resistance. Their range of application continues to expand due to the development of high-quality glasses that are difficult to melt, such as the glass used in liquid crystal display panels. This type of glass is produced at high temperatures, and thus the platinum alloys employed are required to have high strength. Therefore, a platinum–rhodium alloy strengthened with about 10 wt% of rhodium solid solution is used, while oxide dispersion-strengthened (ODS) platinum alloys have also been developed and applied to satisfy even higher strength requirements [2, 3]. ODS platinum alloys are materials comprising zirconium oxide particles dispersed in platinum or a platinum–rhodium alloy matrix, where the dispersed particles enhance the high-temperature strength, suppress the grain growth, and impart long-term stable characteristics [4]. These components are very expensive and the longest possible lifetime with the least amount of usage is required, so it is necessary to extend the lifetime while also considering the production cost. In particular, a melting crucible with a stirrer is a complex environment where hoop stress is generated by the internal pressure from the molten glass on the wall of the melting crucible and pressure fluctuations occur due to the movements of the

stirrer blade. It is assumed that the hoop stress due to the internal pressure by the molten glass causes creep damage and that the repeated bending stress because of pressure fluctuations leads to fatigue damage. However, it is very difficult to estimate the lifetime accurately because it is necessary to examine the interaction between creep and fatigue. Few data are available regarding the mechanical properties of these alloys at high temperatures, although some studies have investigated their creep properties under high temperature fatigue [4-6]. Thus, the effects of the mean interparticle distance and grain aspect ratio with respect to high-temperature fatigue have been investigated, and it was shown that the fatigue strength is greater when the mean interparticle distance is smaller and the grain aspect ratio is larger [7]. However, the interaction between creep and fatigue remains unclear. Therefore, it is difficult to estimate the effects of the hoop stress due to the internal pressure from the molten glass and the cyclic bending stress because of the rotation of the stirrer on the lifetime of the platinum alloy container used in the stirring process.

The interactions between creep and fatigue have been investigated extensively at high temperatures for Ni-based alloys, ODS-Ni-based alloys, and stainless steels, and methods for predicting their lifetimes have also been developed [8-15]. In these studies, the relationships between creep, fatigue damage additivity, and fracture morphology were determined using the linear damage rule and ductility exhaustion rule, and the effects on the lifetime of the materials because of hardening due to repeated loading were determined. However, the operating temperature range for these alloys is limited to about 60% of the melting point due to the problem of high-temperature oxidation. Platinum alloys are used in the temperature range exceeding 80% of the melting point, so it is considered that the phenomena may be different. Hence, it is difficult to apply these findings directly. Therefore, in the present study, we used zirconium ODS platinum–10% rhodium alloy as the test material, which was employed to make the container for the stirring process. Bending fatigue testing was conducted at 1400 °C (similar to the actual environment) in the state where the axial stress simulated the hoop stress in order to elucidate the fatigue properties and to clarify the fracture mechanism.

## **2. Experimental studies**

### **2-1. Materials**

The test material was platinum-10 wt% rhodium alloy dispersed with 0.16 wt% zirconium oxide particles (FKS® Rigilit®, Umicore AG & Co. KG), and its physical properties are listed in Table 1. The test pieces were cut from a sheet of material with a thickness of 0.8 mm using an electrical discharge machining and a notch was made in the part that experienced a high temperature during the test, as shown in Fig. 1. And the direction of the hoop stress generated in the container used for the stirring process was made to coincide with the axial direction of the test piece. Further, the rolling direction was parallel to the axial direction of the test piece. After processing, all the pieces

**Table 1.** Mechanical Properties of ODS Pt–10%Rh.

Temperature [°C]	Tensile Strength [MPa]	Young's Modulus [GPa]	Poisson's ratio
20	430.5	200	0.261
1400	71.5	122	0.247

were annealed at 1300 °C for 1 h to prepare them for the test.

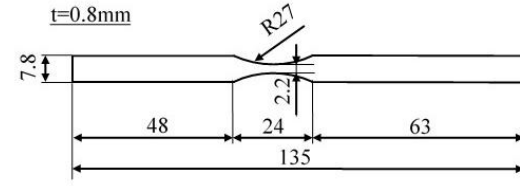


**Fig. 1.** Shape of the specimen.

## 2-2. High-temperature bending fatigue test with axial stress

A bending fatigue testing machine (PTF-160, Tokyo Koki Co. Ltd) was used for the test. As shown in Fig. 2, one side of the test piece was subjected to a certain axial stress as a minimum tensile stress ( $\sigma_{\min}$ ) and the test was conducted with a stress waveform similar to that in an actual environment by applying a cyclic bending stress amplitude ( $\sigma_a$ ). At this time point, the test piece was completely fixed by Jig B, but it was not restrained in the axial direction by Jig A, and there was gap of 0.1 mm above and below the test piece. The stress conditions occurred in cross sections (A), (B), and (C) of the test piece shown in Fig. 2, which was assumed to be an elastic body, and schematic images are presented in Fig. 3. Axial tensile stress was applied so the stress ratio differed according to the position in the direction of the thickness, even in the pulsating fatigue test. Tension–tension loading was repeated with a positive stress ratio on the tension side (A). A constant stress due to axial stress was loaded on the central part of the direction of thickness (B). Tension–compression loading was repeated with a negative stress ratio on the compression side (C). As mentioned above, Fig. 3 shows the stress state assuming that the test piece is an elastic body and, as explained in detail in Section 4, it should be noted that different stress conditions existed because plastic deformation occurred depending on the test conditions. The waveform used for the test was a sine wave with displacement control and the test frequencies were  $f = 5, 12.5,$  and  $20$  Hz. An electric furnace with a molybdenum disilicide heating element was installed at the center of the test piece, where the center of the notch was maintained at 1400 °C and the test was performed under air. To obtain the creep rupture strength diagram for this material, a uniaxial creep test was also conducted where various axial stresses were applied using the aforementioned testing machine.

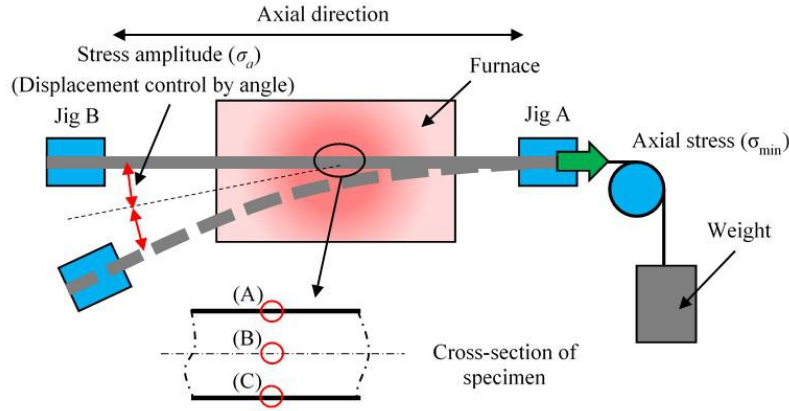


**Fig. 2.** Schematic of the bending fatigue test with axial stress.

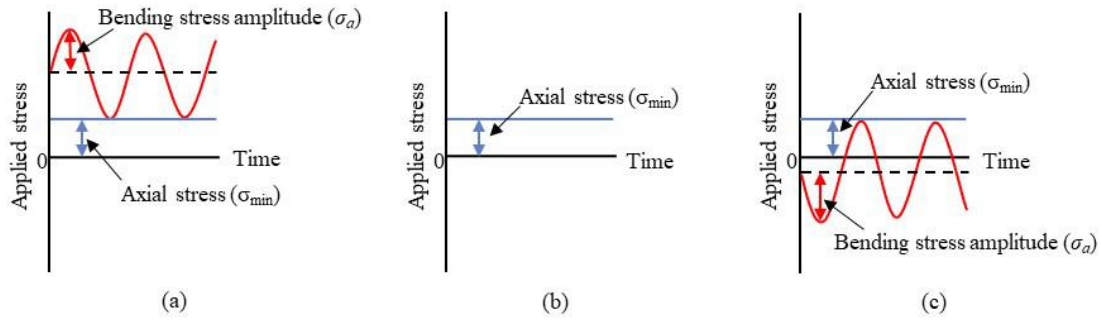


**Fig. 3.** Theoretical images of stress applied to the specimen. (a) Applied stress at position (A). (b) Applied stress at position (B). (c) Applied stress at position (C).

### 2-3. Finite element method (FEM) analysis

To evaluate the distribution of the stress and strain generated in the notch during the test, FEM analysis was performed using ABAQUS. The analysis used an eight-node hexahedron non-conforming element comprising 5220 nodes and 3680 elements. And it is a half model divided into two parallel to the axial direction at the center of the test piece. About the mesh size around the center of the test piece, the longitudinal direction was divided every 1 mm, and the width direction was divided into four in a half model, and the thickness direction was divided into eight. Moreover, based on the temperature distribution in the test piece, as shown in Fig. 4(a), the analysis was performed by considering the temperature dependences of the physical properties. To obtain the temperature measurements, the tip of the type R thermocouple was brought into contact with the test piece and the measurement was acquired while moving 2.5 mm on each test piece, and the distribution was then determined. However, the temperature of the area in contact with the jig could not be measured, so 200 °C was treated as the temperature of the relevant area, which was the average temperature inside the jig. Figure 4(b) shows the constraint conditions. The part corresponding to Jig B in Fig. 2 was completely constrained and a rigid body was provided with a

gap of 0.1 mm above and below the test piece, as employed in the actual test for Jig A. As a consequence, the side of Jig A was restricted only in the width direction and not in the axial direction.

The stress amplitude in the high-temperature bending fatigue test with an applied axial stress was set using the value calculated by elastic analysis. The stress was a virtual elastic stress and it was assumed that the specimen did not yield.

However, depending on the stress amplitude, it was assumed that yielding would occur during the test and that creep deformation would also occur because of the high temperature, and thus elastic–plastic creep analysis was also conducted to consider the fracture mechanism. The model shown in Fig. 4(b) was again employed in the elastic–plastic creep analysis and the von Mises condition was used as the yield condition. In order to analyze the behavior of the yield stress and work hardening, the stress–strain diagram shown in Fig. 5 was measured at room temperature and at 1400 °C, and then converted into the true stress for analysis, where the temperature between them was linearly complemented. The creep rate employed for creep analysis was obtained from a previously reported study of the same material and the temperature dependence based on Norton's law [16].

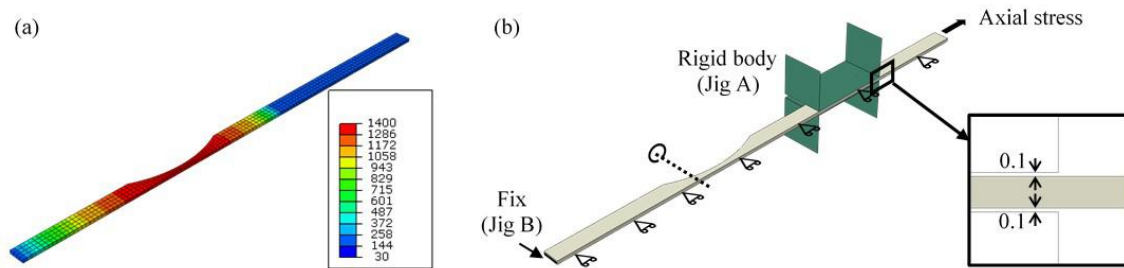


**Fig. 4.** Conditions employed for FEM analysis. (a) Temperature distribution in the specimen based on the measured values. (b) Schematic image of the constraint conditions.

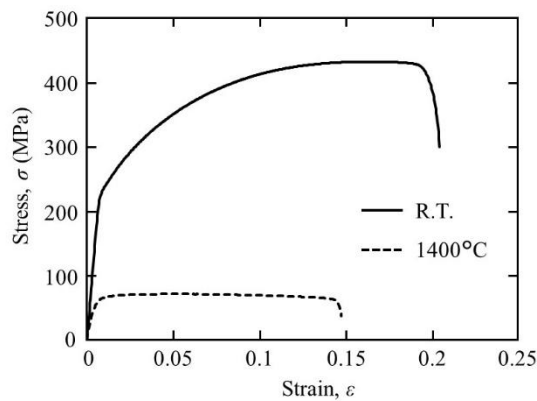


**Fig. 5.** Stress–strain diagram for the ODS platinum-10 wt% rhodium alloy at room temperature and 1400 °C.

## 2-4. Observations

Electrolytic etching and crystal orientation analysis using the electron backscatter diffraction (EBSD) method were conducted to determine the grain structure in the specimen. To study the failure mechanism, the fractured surfaces of the specimens and the internal cross sections were observed using a scanning electron microscope and optical microscope, respectively.

## 3. Results

### 3-1. Structure observations

Figure 6 shows the grain structure of the test piece determined using optical microscopy and the EBSD method after etching. The microstructure observations confirmed that the grain size in the test piece was several tens of microns in the direction of thickness and several tens of microns to 200  $\mu\text{m}$  in the planar direction, where the grain was flat in the direction of thickness for the test piece. The average grain size of the specimen surface measured from the EBSD image was 29.7  $\mu\text{m}$ . In addition, the crystal orientation was in a random state and the material was in a homogeneous state.

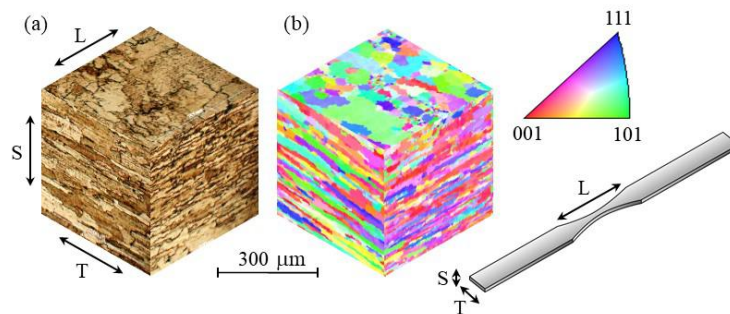


**Fig. 6.** Observations of the test piece. (a) Metal structure observed by optical microscopy. (b) Inverse pole figure (IPF) map obtained by EBSD analysis indicating the crystallographic orientation to the normal to each plane.

### 3-2. Uniaxial creep test

The uniaxial creep test was conducted by applying only an axial stress under air at 1400 °C, and the relationship between the stress and creep rupture time is shown in Fig. 7. Thus, the relationship between the applied stress and rupture time could be represented as a linear relationship in a double logarithmic graph, as in the general creep test for this test system. Figure 8 shows the fractured surface after 161.7 h under an applied stress at 23.4 MPa. The fractured sample exhibited intergranular fracture and it was a typical creep fracture surface with many voids at the grain

boundaries. Wedge- and round-type voids are known to be formed at the grain boundaries in creep fractures [17], and both types of voids were found on the creep fracture surface in this test. In addition, even after the creep test, the initial grain size and grain aspect ratio were maintained by the effect of the dispersed particles, and we considered that there was almost no change in the creep characteristics during the test [18-24].

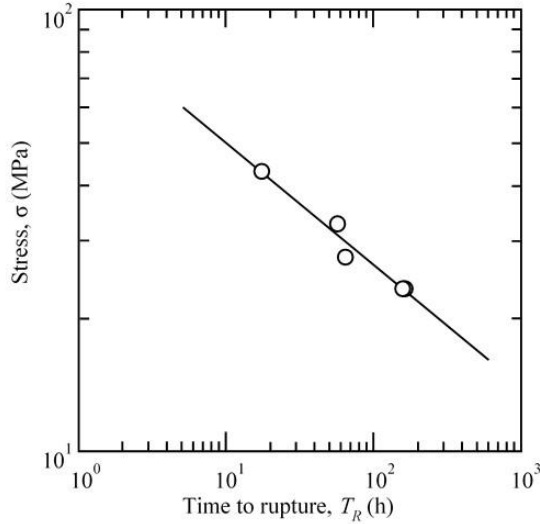


**Fig. 7.** Uniaxial creep test results obtained at 1400°C.

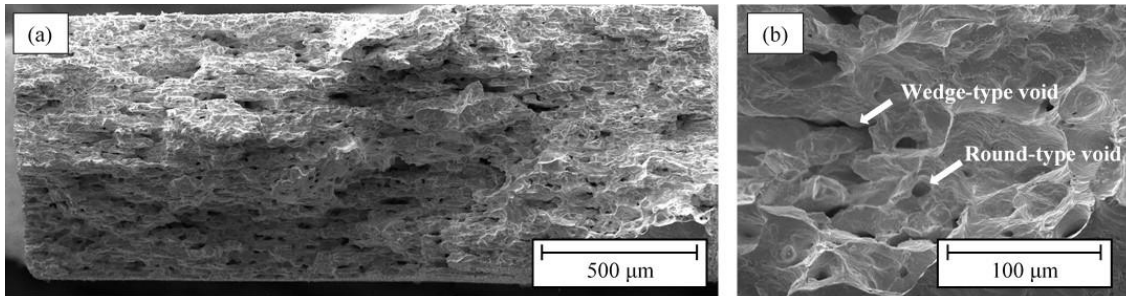


**Fig. 8.** Scanning electron microscopy images of the fracture surface for the uniaxial creep test specimen ( $\sigma = 23.4$  MPa, 161.7 h). (a) Whole fracture surface, and (b) a region in Fig. 8 (a) at a higher magnification.

### 3-3. Effect of frequency on the high-temperature bending fatigue test with axial stress

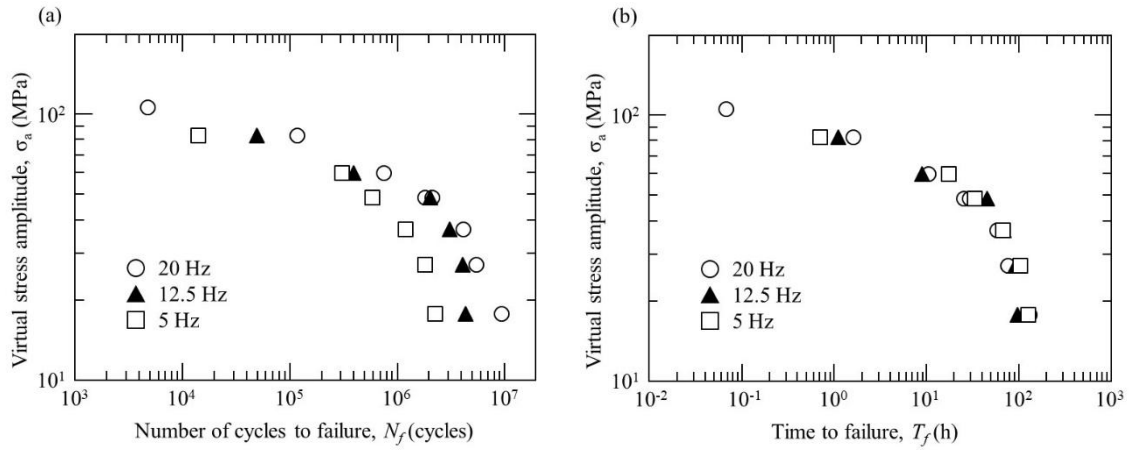
Based on the results of the uniaxial creep test, 23.4 MPa was set as the axial stress because the creep rupture time at 23.4 MPa was close to the time required to apply  $10^7$  repetitive loads at 20 Hz. This stress value is higher than the stress level that can occur in the actual equipment, but it was set to

determine the influence of the axial stress. Figure 9(a) shows the results obtained in the high-temperature bending fatigue tests conducted at frequencies of  $f = 5, 12.5$ , and  $20$  Hz by applying an axial stress at  $23.4$  MPa. The vertical axis was the stress amplitude on the surface of the center of the notch calculated by FEM analysis using the Young's modulus corresponding to the temperature distribution in the furnace in the testing machine. However, it was a virtual elastic stress and we assumed that the specimen did not exhibit plastic deformation. The horizontal axis represents the number of cycles when the test piece was completely separated. Figure 9(a) shows that the fatigue lifetime tended to be shorter at a lower frequency than a higher frequency. In general, it is known that high-temperature fatigue is not independent of the effects of creep, and that frequency dependence occurs [25]. In particular, a high axial stress was applied in this test and we inferred that the effect was more pronounced. The result obtained for a horizontal axis corresponding to the time when the test piece was broken is shown in Fig. 9(b). Clearly, the time dependency was strong because the difference in the fatigue lifetime according to the frequency was almost eliminated when the time to failure was considered. This result suggests that creep strongly affects the fracture mechanism. The test results presented in the double logarithmic graph in Fig. 9(b) show that the virtual stress amplitude and failure time did not have a linear relationship, where the curve bent downward as the stress amplitude decreased. Thus, the dependence of the stress amplitude on the failure time was great in the high stress amplitude test, whereas the dependence was low in the low stress amplitude test. The uniaxial creep rupture time of about  $160$  h when only an axial stress of  $23.4$  MPa was applied demonstrated that the rupture time was close to about  $160$  h as the stress amplitude decreased.

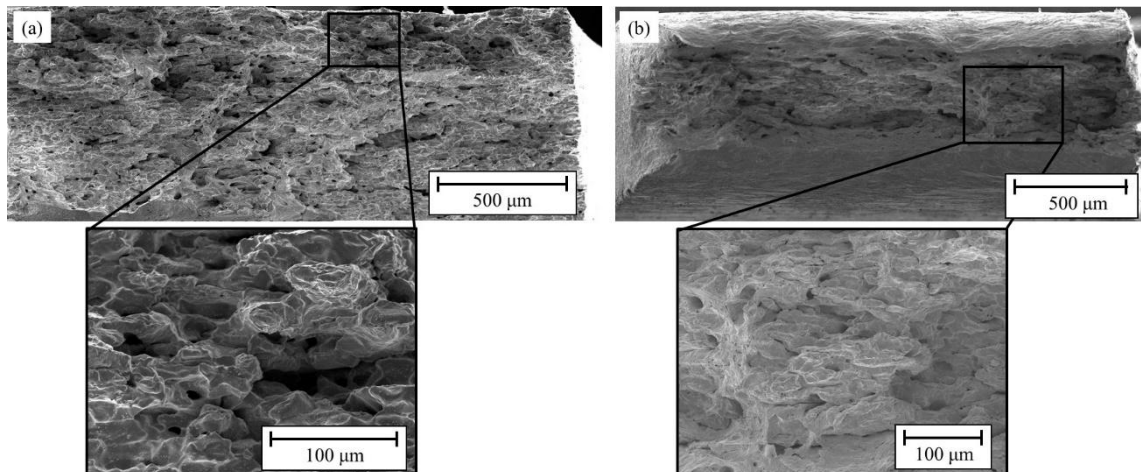
We investigated the fractured surface of the specimen using scanning electron microscopy after the high-temperature bending fatigue test under an axial stress of  $23.4$  MPa at  $f = 20$  Hz, and the results obtained are shown in Fig. 10. In Fig. 10, the results are shown for the fracture surface when the stress amplitude was (a)  $\sigma_a = 17.8$  MPa and (b)  $\sigma_a = 82.9$  MPa. After the low stress amplitude test, i.e.,  $\sigma_a = 17.8$  MPa, intergranular fracture and void formation in the grain boundary were observed, and the sample exhibited the same fracture surface due to creep as that shown in Fig. 8. After the high stress amplitude test, i.e.,  $\sigma_a = 82.9$  MPa, a creep fracture surface appeared near the center of the direction of thickness for the test piece. However, necking due to plastic deformation was observed near the upper and lower surfaces of the test piece. This surface fracture morphology is clearly different from that observed for high-temperature fatigue fractures in stainless steel and nickel-based ODS alloys, thereby suggesting that a different fracture mechanism occurs [26-29]. Figure 11 shows cross-sectional observations of the fractured part of the test piece after the test, where Figs 11(a) and 11(b) present the results obtained at  $\sigma_a = 17.8$  and  $82.9$  MPa, respectively. When the stress amplitude was small, i.e.,  $\sigma_a = 17.8$  MPa, a clear intergranular fracture and voids were observed at the grain boundary in the entire region in the test piece. However, the morphology



of these voids was slightly different from the fine void formation and connections in the grain boundaries due to high-temperature fatigue in other alloys [30, 31], although the wedge- and round-type voids observed for creep damage were present. When the stress amplitude was large, i.e.,  $\sigma_a = 82.9$  MPa, the grain boundary fracture was limited near the center of the direction of thickness for the fracture surface, and necking due to plastic deformation occurred near the upper and lower surfaces. In addition, there were many creep voids near the center of the direction of thickness in a similar manner to those in the low stress amplitude test, but few were generated in the part where plastic deformation occurred in the upper and lower surfaces. We considered that there was a correlation between the change in the fracture surface morphology, the occurrence of creep voids, and the dependency of the stress amplitude on the failure time. We attempted to elucidate the fracture mechanism based on stress distribution analysis using FEM.



**Fig. 9.** Results of bending fatigue test under axial stress at 1400°C. (a) Horizontal axis represents the number of cycles to failure, and (b) horizontal axis represents the time to failure.



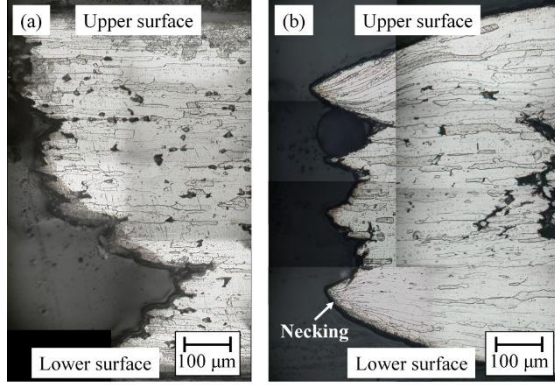


**Fig. 11.** Cross-sectional observations after bending fatigue test under axial stress at: (a)  $\sigma_a = 17.8$  MPa and (b)  $\sigma_a = 82.9$  MPa.

#### 4. Discussion

Figure 12 shows the results obtained after elastic–plastic creep analysis using FEM to confirm the stress generated in the test piece during the test. The stress distributions in the 10th cycle are shown for the cross-sections of the test pieces at: (a)  $\sigma_a = 17.8$  MPa, (b)  $\sigma_a = 36.9$  MPa, and (c)  $\sigma_a = 82.9$  MPa under an axial stress of 23.4 MPa. In each panel, the upper part shows the distribution at the maximum bending load and the lower part shows the distribution after the sample returned to its straight position. The comparison was conducted for the 10th cycle because when yielding occurred, the ratio of the elastic strain relative to the inelastic strain changed in the first few cycles, and the stress distribution then changed in each cycle. However, the 10th cycle was treated as representative because the ratio was regarded as almost constant after that cycle. The results showed that at  $\sigma_a = 17.8$  MPa, tensile stress was generated on the upper half or more of the area of the test piece during bending, and only axial stress acted during the return; therefore, the distribution of the tensile stress became uniform in the direction of thickness. The tensile stress was generated on the upper half or more of the area during bending because a neutral axis was present below the center of the direction of thickness due to the application of axial stress.

By contrast, at  $\sigma_a = 36.9$  MPa, a high tensile stress greater than the axial stress remained near the center of the direction of thickness even at the time of the return to a straight position. This result was obtained because a compressive stress was generated in the vicinity of the upper surface during

the return due to the yield of the upper area during bending, and a tensile stress greater than the axial stress was generated as a reaction force around the center of the direction of thickness, which acted as a residual stress [32, 33]. When the stress amplitude increased further, at  $\sigma_a = 82.9$  MPa, the upper half area of the test specimen and the area near the lower surface yielded greatly to the tensile and compression sides, respectively, during bending. In addition, while returning, the lower half or more of the area yielded to the tensile side, whereas the area near the upper surface yielded to the compression side. Thus, tension–compression greater than the yield stress was repeated near the upper and lower surfaces, but a high tensile stress was always applied around the center of the direction of thickness because of the large yield of the upper and lower surfaces during both bending and the return. Figure 13 shows the stress generated at the center of the direction of thickness during the test from the first to the fifth cycles. The horizontal axis in Fig. 13 represents the number of cycles with a repeated bending load, where bending and returning were repeated every 0.5 cycles. A substantially constant tensile stress continued to be applied regardless of the bending and return, and the value increased with the stress amplitude.

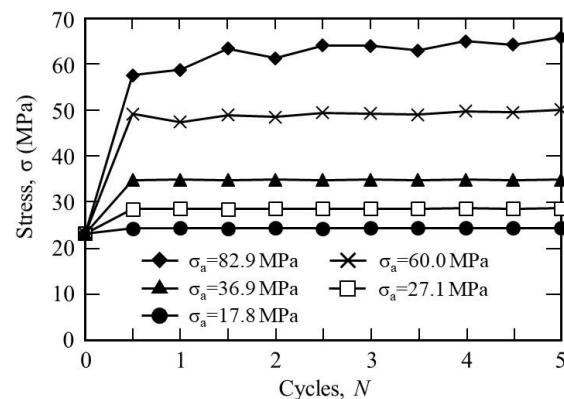
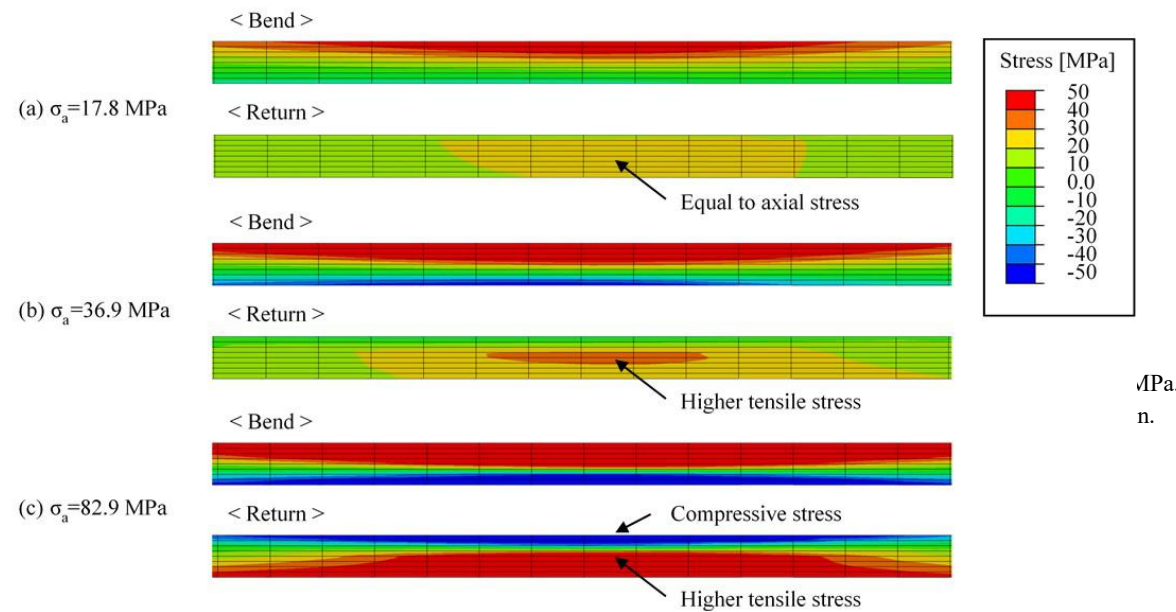


**Fig. 13.** Stress generated at the center of the direction of thickness according to FEM analysis.

When a high tensile stress was continually applied at high temperatures, creep damage was expected to progress in the corresponding region. Figure 14 shows the relationship between the estimated creep rupture time calculated from Fig. 7 using the stress generated at the center of the direction of thickness on the vertical axis and the actual rupture time on the horizontal axis. The rupture time for the test piece matched very well with the creep rupture time for the stress generated at the center of the direction of thickness, thereby suggesting that the internal creep fracture was strongly related to the fracture during high-temperature bending fatigue under a relatively high axial stress. To clarify the failure process, Fig. 15 shows a cross-sectional image of both sides of the test piece fractured under an axial stress of 23.4 MPa and  $\sigma_a = 82.9$  MPa. Many creep voids were present in the central part of the direction of thickness near the fractured part. However, no creep voids were generated near the upper and lower surfaces, probably due to the suppression of creep void formation during the compression half cycles because cyclic tension–compression stress was applied near the upper and lower surfaces [34]. Note that even after the high-temperature bending fatigue test with axial stress, the initial grain size and grain aspect ratio were maintained, and it was considered that there was almost no change in the creep characteristics during the test. In the fractured surface shape, the central part of the direction of thickness was recessed compared with that near the upper and lower surfaces, which were in a state of necking and stretching. Based on these results, we suggest that the high tensile stress generated near the central part of the direction of thickness caused the internal creep failure, and the failure then propagated to near the upper and lower surfaces where the true stress increased.

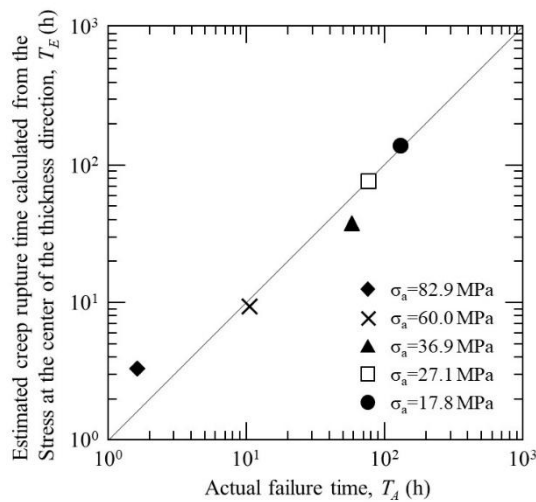


**Fig. 14.** Relationship between creep rupture time estimated from the stress at the center of the direction of thickness and the actual failure time.

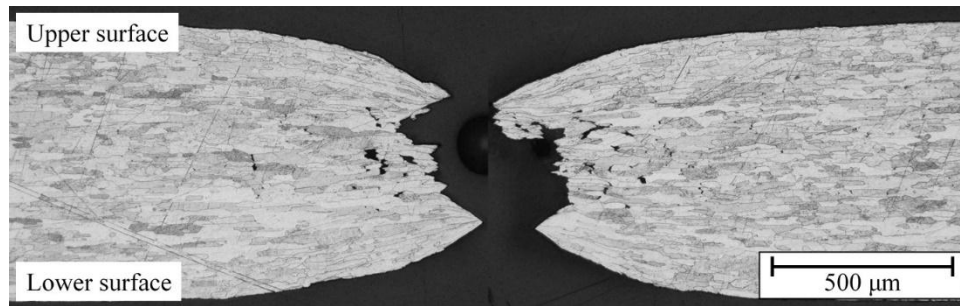


**Fig. 15.** Cross-sectional image obtained after the bending fatigue test with axial stress ( $\sigma_a = 82.9$  MPa).

Based on the results described above, the failure mechanisms that occurred under high-temperature fatigue when subjected to a relatively high axial stress can be summarized as follows. First, in the low stress amplitude test, the effect of the axial stress applied was always greater than that of the cyclic stress, and thus the conditions were similar to uniaxial creep, where creep voids were generated and they connected over the entire direction of thickness. By contrast, in the high stress amplitude test, the areas near the upper and lower surfaces yielded because of the cyclic bending deformation. Hence, high tensile stress was continually applied to the central part of the direction of thickness, and creep voids were generated and connected to cause earlier internal failure. The process where a crack propagated to the surface side as the load stress increased was also considered. The failure mechanism differed between the low stress amplitude test and the high stress amplitude test, and thus the virtual stress amplitude and the failure time did not have a linear relationship, as shown by the double logarithmic graph in Fig. 9, where the curve bent downward as the stress amplitude decreased. Therefore, it is possible to predict the lifetime with high accuracy during high-temperature bending fatigue for an ODS Pt–Rh alloy when subjected to a relatively high axial stress by evaluating the presence or absence of yield due to the stress amplitude, as well as the stress generated in the central part of the direction of thickness.

## 5. Conclusions

In this study, we conducted high-temperature bending fatigue tests using an ODS platinum–rhodium alloy at 1400 °C with a relatively high axial stress and the results demonstrated the following.

- (1) A higher test frequency corresponded to a higher number of cycles until failure. However, the rupture time was not dependent on the frequency, but instead fracturing depended on the time.
- (2) At a low stress amplitude, the effect of the cyclic stress was small and creep damage progressed

throughout the cross-section of the test sample due to axial stress. However, at a high stress amplitude, creep damage progressed only in the central part of the direction of thickness and fracturing originated from inside the sample.

(3) FEM analysis showed that when the stress amplitude was high, high tensile stress remained inside the sample due to the yielding near the surface. Hence, the creep damage progressed inside the sample and resulted in breakage.

(4) It is possible to predict the lifetime with high accuracy under high-temperature bending fatigue when subjected to a relatively high axial stress by evaluating the presence or absence of yielding due to the stress amplitude and the stress generated in the central part of the direction of thickness.

## References

- [1] T. Okabe, Current Status of Platinum Group Metals and Recycling Technologies, *Materia Jpn.* 46 (2007) 522-529.
- [2] G. L. Selman, J. G. Day, A. A. Bourne, Dispersion Strengthened Platinum, *Platinum Metals Rev.* 18 (1974) 46-57.
- [3] G. L. Selman, A. A. Bourne, Dispersion-Strengthened Rhodium-Platinum, *Platinum Metals Rev.* 20 (1976) 86-90.
- [4] N. Sekido, A. Hoshino, M. Fukuzaki, Y. Yamabe-Mitarai, T. Maruko, Steady state creep behavior of zirconia dispersion strengthened platinum alloys in medium stress regime, *Mater. Sci. Eng. A* 528 (2011) 8451-8459.
- [5] B. Fischer, A. Behrends, D. Freund, D. F. Lupton, J. Merker, High Temperature Mechanical Properties of the Platinum Group Metals, *Platinum Metals Rev.* 43 (1999) 18-28.
- [6] K. Murayama, H. Yamasaki, T. Hamada, High-temperature creep of GTH (Gottsu-Tsuyoi-Hakkin), *Mater. Sci. Eng. A* 510-511 (2009) 312-316.
- [7] S. Hitomi, H. Suzuki, Improvement in High Temperature Fatigue Strength of Industrial Oxide Dispersion Strengthened Platinum with Formation of Stretched Coarse Grain Structure, *Trans. Jpn. Soc. Mech. Eng. A* 71 (2005) 1383-1389.
- [8] W. O. Ngala, H. J. Maier, Creep-fatigue interaction of the ODS superalloy PM 1000, *Mater. Sci. Eng. A* 510-511 (2009) 429-433.
- [9] S. Taira, R. Koterazawa, M. Inoue, Fatigue and Dynamic Creep Properties of 13 Cr Steel at Elevated Temperature under Combined Stresses of Static Tension and Alternating Bending, *Bulletin of JSME* 2 (1959) 508-513.
- [10] K. Yagi, K. Kubo, C. Tanaka, Effect of Creep Stress on Creep-Fatigue Interaction for SUS 304 Austenitic Steel, *J. Soc. Mater. Sci., Jpn.* 28 (1979) 400-406.
- [11] K. Yagi, K. Kubo, C. Tanaka, Evaluation of Creep Fatigue Interaction by Linear Damage Rule and Appearance of Fracture for SUS 304 Stainless Steel Subjected to Combined Creep-Fatigue

- Tests, J. Soc. Mater. Sci., Jpn. 29 (1980) 928-934.
- [12] M. Yamauchi, Y. Chuman, T. Otani, Y. Takahashi, Study on the Effect of Prior Fatigue and Creep-Fatigue Damage on the Fatigue and Creep Characteristics of 316 FR Stainless Steel, Trans. Jpn. Soc. Mech. Eng. 67 (2001) 60-65.
- [13] N. Matsuda, S. Umezawa, H. Miyata, A New Prediction Method of Fatigue-Creep Interaction Behavior Based on Total Strain Energy for High Strength Super Alloy, J. Soc. Mater. Sci., Jpn. 38 (1989) 809-815.
- [14] B. Fourniera, F. Dalle, M. Sauzay, J. Longour, M. Salvi, C. Caes, I. Tournie, P.-F. Giroux, and S.-H. Kim, Comparison of various 9–12%Cr steels under fatigue and creep-fatigue loadings at high temperature, Mater. Sci. Eng. A 528 (2011) 6934-6945.
- [15] K. Miyamoto and T. Ogata, Damage Process and Measurement of Crystal Misorientation by EBSD under Creep and Creep Fatigue Conditions on Ni Base Alloy HR6W, J. Soc. Mater. Sci., Jpn. 68 (2019) 614-621.
- [16] Reppich, B., Brungs, F., Hümmer, G., and Schmidt, H., Modelling of the Creep Behaviour of ODS Platinum-Based Alloys, in Proceedings of the 4th International Conference on Creep and Fracture of Engineering Materials and Structures, edited by R.W. Evans and B. Wilshire, The Institute of Metals, 142-158 (1990).
- [17] K. Yagi, C. Tanaka, K. Kubo, Correlation between Creep-Fatigue Interaction and Creep Fracture Mode for SUS 316 Stainless Steel Subjected to Combined Creep-Fatigue Loading, J. Soc. Mater. Sci., Jpn. 33 (1984) 1533-1539.
- [18] T Hamada, S Hitomi, Y Ikematsu, S Nasu, High-Temperature Creep of Pure Platinum, Mater. Trans. 37 (1996) 353-358.
- [19] J. D. Whittenberger, Creep and Tensile Properties of Several Oxide Dispersion Strengthened Nickel Base Alloys, Metall. Trans. A 8 (1977) 1155-1163.
- [20] R. Ohtani, T. Kitamura, H. Miki, Crack Propagation of Oxide Dispersion Strengthened Superalloy Inconel MA754 in Creep-Fatigue, J. Soc. Mater. Sci., Jpn. 40 (1991) 1297-1302.
- [21] M. Heilmaier, B. Reppich, Creep Lifetime Prediction of Oxide-Dispersion-Strengthened Nickel-Base Superalloys: A Micromechanically Based Approach, Metall. Mater. Trans. A 27 (1996) 3861-3870.
- [22] N. Miura, N. Harada, Y. Kondo, M. Okabe and T. Matsuo, Stress Exponent of Minimum Creep Rate and Activation Energy of Creep for Oxide Dispersion-strengthened Nickel-based Superalloy MA754, ISIJ Int. 52 (2012) 140-146.
- [23] H. R. Z. Sandim, A. O. F. Hayama and D. Raabe, Recrystallization of the ODS superalloy PM-1000, Mater. Sci. Eng. A 430 (2006) 172-178.
- [24] S. C. Ur, S. Suh and P. Nash, Creep in Grain Coarsened ODS MA NiAl, Met. Mater. Int. 8 (2002) 333-339.

- [25] S. Taira, R. Ohtani, T. Kitamura, K. Yamada, J-Integral Approach to Crack Propagation under Combined Creep and Fatigue Condition, *J. Soc. Mater. Sci., Jpn.* 28 (1979) 414-420.
- [26] E. Vasseur, L. Rémy, High temperature low cycle fatigue and thermal-mechanical fatigue behaviour of an oxide-dispersion-strengthened nickel-base superalloy, *Mater. Sci. Eng. A* 184 (1994) 1-15.
- [27] W. Hoffelner, R. F. Singer, High-Cycle Fatigue Properties of the ODS-Alloy MA 6000 at 850°C, *Metall. Trans. A* 16 (1985) 393-399.
- [28] K. Kobayashi, K. Yamaguchi, M. Hayakawa, M. Kimura, High-temperature fatigue properties of austenitic superalloys 718, A286 and 304L, *Int. J. Fatigue*. 30 (2008) 1978-1984.
- [29] L. Straßberger, A. Chauhan, T. Gräning, S. Czink and J. Aktaa, High-temperature low-cycle fatigue behavior of novel austenitic ODS steels, *Int. J. Fatigue*. 93 (2016) 194-200.
- [30] R. P. Skelton, The growth of grain boundary cavities during high temperature fatigue, *Philos. Mag.* 14 (1966) 563-572.
- [31] A. Gittins, The Mechanism of Cavity Growth in Copper during High-Temperature Fatigue, *Met. Sci.* 2 (1968) 51-58.
- [32] R. Udo, H. Nishikawa, H. Hato, K. Miyazaki, K. Masaki, H. Numakura, Effect of Loading Method and Mean Stress on Fatigue Strength of Super Duplex Stainless Steel, *Tetsu-to-Hagané* 103 (2017) 201-207.
- [33] S. Taira, Y. Murakami, R. Koterazawa, Dynamic Creep of Low Carbon Steel at Elevated Temperature as Related with the Residual Stresses Retained after Dynamic Creep under Combined Stresses of Static Tension and Alternating Bending, *J. Jpn. Soc. Test. Mat.* 8 (1959) 781-786.
- [34] R. Ohtani, T. Kitamura, W. Zhou, Effect of Compressive Creep on Crack Propagation of Type 304 Stainless Steel under Time-Dependent Creep-Fatigue Conditions, *J. Soc. Mater. Sci., Jpn.* 40 (1991) 1290-1296.